Applied Catalysis B: Environment and Energy 352 (2024) 124045

Contents lists available at ScienceDirect

Applied Catalysis B: Environment and Energy

journal homepage: www.elsevier.com/locate/apcatb

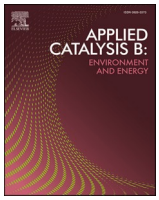

Boron-doped Cu-Co catalyst boosting charge transfer in photothermal carbon dioxide hydrogenation

Jiaqi Wang [a,b], Shuangjun Li [b], Jingjing Zhao [b], Kaihong Liu [b], Bo Jiang [b,*], Hexing Li [a,b,**]

[a] School of Chemistry and Molecular Engineering, East China University of Science and Technology, 130 Meilong Road, Shanghai 200237, China
[b] Chinese Education Ministry Key Lab and Joint International Research Lab of Resource Chemistry, Shanghai Frontiers Science Center of Biomimetic Catalysis, College of Chemistry and Materials Science, Shanghai Normal University, Shanghai 200234, China

ARTICLE INFO

Keywords:
Photothermal catalysis
CO_2 hydrogenation
Synergistic effect
Heterojunction catalysts
Boron-doped Cu-Co catalyst

ABSTRACT

Photothermal catalysis of CO_2 hydrogenation holds great potential in achieving carbon neutrality. However, the rational design of cost-effective photothermal catalysts with high performance for CO_2 hydrogenation is an ongoing challenge. Herein, we employed $CuCo_yBO_x$ composite catalysts by incorporating both $CuBO_x$ and amorphous $CoBO_x$ to efficiently catalyze the CO_2 hydrogenation. Besides the high selectivity (98.0%), the optimized $CuCo_5BO_x$ demonstrated a remarkable CO yield of 124.7 mmol g^{-1} h^{-1} under illumination at 300°C, which was 3 times higher than the traditional thermocatalysis. Experimental results and theoretical calculations demonstrated $CuBO_x$ acted as a photocatalyst, donating electrons to $CoBO_x$ active sites. Coupling boron-oxygen species with CuCo bimetallic-oxides synergically enhanced the CO_2 adsorption capacity and accelerated charge transfer, thereby enhancing the photothermal synergistic effect and consequently boosting the catalytic activity. This study establishes an approach for the rational design of non-precious metal-boride catalysts, enabling efficient photothermal conversion of CO_2 into CO under mild conditions.

1. Introduction

Heterogeneous CO_2 hydrogenation to manufacture high-value chemicals using green H_2 represents a promising approach for alleviating both the energy crisis and environmental pollution.[1] However, the conventional thermal activation of CO_2 is an energy-intensive process that demands high pressure and temperature to break the C═O bonds.[2] In contrast, as an alternative method, photocatalytic CO_2 reduction presents a green and sustainable strategy. It utilizes photo-excited electrons from semiconductors to activate CO_2 but suffers from a low production rate, thus limiting its practical application.[3,4] It is crucial to explore an efficient and energy-saving method for CO_2 hydrogenation. Recently, photothermal CO_2 hydrogenation, integrating the advantages of both photocatalysis and thermocatalysis, has demonstrated the potential to significantly improve catalytic performance by partially offsetting the dependence on fossil fuel energy. Ye et al. demonstrated an excellent photothermal effect of Group VIII metals for CO_2 hydrogenation, especially with the Ru/Al_2O_3 and Rh/Al_2O_3 catalysts, showing a high CO_2 conversion and CH_4 selectivity.[5] Hydride-terminated Si nanoparticles with 3.5 nm diameter on average were reported by Ozin et al. for catalyzing CO_2 hydrogenation to CO at μmol g^{-1} h^{-1} scale under photothermal catalysis.[6] Moreover, the ability of photothermal CO_2 hydrogenation can be further optimized by introducing metal-active sites such as Ru, Pt, Ni, *et al.*[7–9] Despite some progress, the rational exploration of cost-effective photothermal catalysts with high performance remains challenging.

To date, a variety of metal oxide-based photocatalysts such as In_2O_3, Cu_2O, and TiO_2 have been developed toward the reverse water-gas shift (RWGS: $CO_2+H_2 \rightarrow CO+H_2O$ $\Delta H_{298\ K} = +41.2$ kJ mol^{-1}) reaction at atmospheric pressure.[10,11] Among them, Cu-based oxides, a low-cost semiconductor, have garnered enormous attention. However, the performance and stability of Cu-based oxide catalysts still fell short of satisfactory levels due to rapid carrier recombination, poor light adsorption ability, and catalyst sintering during the reaction.[12] Recent advances reported that boron doping in Cu-based materials modifies the electronic structures of active centers and works as guest elements for accelerating charge transfer between different species.[13] Incorporating transition metal-based materials with boron offers

* Corresponding author.
** Corresponding author at: Chinese Education Ministry Key Lab and Joint International Research Lab of Resource Chemistry, Shanghai Frontiers Science Center of Biomimetic Catalysis, College of Chemistry and Materials Science, Shanghai Normal University, Shanghai 200234, China.
E-mail addresses: jiangbo@shnu.edu.cn (B. Jiang), hexing-li@shnu.edu.cn (H. Li).

https://doi.org/10.1016/j.apcatb.2024.124045
Received 14 February 2024; Received in revised form 29 March 2024; Accepted 4 April 2024
Available online 5 April 2024

opportunities for electrocatalytic hydrogen evolution reactions,[14] electrocatalytic CO_2 reduction,[15] electro-oxidation of formic acid, [16] electrocatalytic oxygen evolution reaction,[17] and so forth. For instance, the introduction of boron into copper-based catalysts exhibit a high Faraday efficiency of ~79% in electrocatalytic reduction of CO_2 into C_2 products as boron modifies the electronic configuration of Cu with stable Cu^+ sites.[15] CoB oxide has been demonstrated as an exceptional electrocatalyst in oxygen evolution reactions compared to Co_3O_4 catalysts.[18] Although great progress has been made in electrocatalysis, the potential of B doping in transition oxides for photothermal CO_2 hydrogenation remains untapped.

Here, we demonstrated boron-doped $CuCo_yBO_x$ heterojunction catalysts comprising $CuBO_x$ and $CoBO_x$ for photothermal RWGS reactions. The boron-oxygen plays dual critical roles in the composite by promoting charge carrier transportation via the intimate interfaces and regulating the electronic configuration of active sites. The optimized sample achieves a CO yield rate of up to 124.7 mmol g^{-1} h^{-1}, showcasing an impressive selectivity of 98% at 300℃ under photothermal catalysis—three times higher than thermal catalysis. Mechanistic studies indicated that boron-doped metal oxides confer significant advantages in terms of CO_2 adsorption and activation. Simultaneously, the mixed valence of Cu^0 and Cu^+ species effectively reduces the energy barrier *via* a photocatalytic pathway. This study presents a novel approach for constructing boron-doping metal oxides for photothermal RWGS reactions.

2. Material and methods

2.1. Catalyst preparation

All the reagents utilized were analytical products purchased from Aladdin without further purification in this study. Typically, the PVP (100 mg) and sodium citrate (50 mg) were completely dissolved in 2 mL of H_2O. Next, $Cu(OAc)_2{\cdot}H_2O$ (4 mL, 0.04 M) and $Co(OAc)_2{\cdot}4\ H_2O$ (y mL, 0.04 M) (y=1–7), and dimethylamine borane (10 mL, 0.5 M) were added to this solution in sequence. The solution was incubated at 30℃ for an additional 4 hours until the reaction color turned black. The Cu-Co bimetallic catalyst, CuCoyB, was obtained by centrifugation and washing with ethanol. Finally, $CuCo_yBO_x$ was obtained by drying $CuCo_yB$ in the air at 25℃ overnight.

The Cu monometallic catalyst was synthesized with the above method and named $CuBO_x$ to explore the impact of metal interaction. The synthesis of the Co monometallic catalyst was triggered by adding a certain amount of $NaBH_4$ solution before incubation. The rest of the process is the same as $CuCo_yBO_x$, and the catalyst was named $CoBO_x$.

2.2. Characterization

The morphologies were characterized by transmission electron microscope (TEM, FEI Tecnai G2 F30, America). The X-ray diffraction pattern (XRD) of the crystalline structure was examined using Cu Kα radiation (Bruker advance D8, Germany), and the scan rate for data recording was set at 0.5° min^{-1}.

X-ray photoelectron spectroscopy (XPS, Thermo Scientific K-Alpha+ spectrometer) characterized the chemical state using a monochromatic Al Kα radiation source. The calibration of all binding energies (BEs) was performed by referencing the C1s peak at 284.8 eV. The N_2 adsorption-desorption isotherms were measured using a Micromeritics ASAP 2010 instrument at a temperature of 77 K. Based on these measurements, the specific surface area (S_{BET}) and pore volume (VP) were determined by using the Brunauer-Emmett-Teller (BET) and Barrett-Joyner-Halenda (BJH) models. The photocurrent tests were conducted at the Shanghai Chenhua CHI760E electrochemical workstation utilizing a three-electrode system. The working electrode consisted of carbon paper coated with the photocatalyst, while Pt was used as the counter electrode. The reference electrode used was Ag/AgCl, and Na_2SO_4 solution (0.5 M) served as the electrolyte. The element analysis was conducted using an inductively coupled plasma optical emission spectrometry (ICP-OES, Agilent ICP-OES 720ES). The UV–visible diffuse reflectance spectroscopy (UV–vis DRS, Shimadzu UV-3600plus) was utilized to identify the absorption of light. High-purity $BaSO_4$ served as a standard reagent for baseline calibration purposes. The temperature-programmed desorption of CO_2 (CO_2-TPD) was measured using a Micromeritics-2920 instrument. The samples were pretreated at 100℃ (5℃ min^{-1}) under He flows (20 mL min^{-1}) for 1 h. Afterwards, the materials underwent a cooling process and were subjected to CO_2 exposure (20 mL min^{-1}) for 1 h at 50℃. Subsequently, measurement was conducted by gradually raising the temperature up to 750℃ with a heating rate of 10℃ min^{-1} under He gas (30 mL min^{-1}). The in-situ reaction chamber of a Nicolet iS10 spectrometer (Thermo Scientific) was utilized for conducting in situ diffuse reflectance infrared Fourier transform (DRIFT), enabling the observation of surface adsorption of intermediates during the course of the reaction process. The reactor was heated to 100℃ and held for 2 h under He gas (20 mL min^{-1}) to eliminate the moisture and surface contaminants from the catalyst. Then, after cooling down the reactor to 25℃ in He gas, CO_2 and H_2 were introduced to explore the experimental mechanism by changing the temperature, radiation, and other conditions.

2.3. Materials testing for the heterogeneous photothermal catalytic hydrogenation of CO_2

As shown in the diagram (Fig. S1-S2), the photothermal CO_2 hydrogenation experiments were carried out on the catalyst in a self-made photothermal multiphase reactor. Mix the catalyst and 0.5 g quartz sand evenly, fill it in the central window of a self-made quartz tube (10 mm×10 mm×2 mm), and fix it with quartz cotton to prevent its scattering. The catalyst was heated to the desired reaction temperature by the electric heating device, and the thermocouple monitors the temperature in real-time. The xenon lamp (Beijing PerfectLight, 300 W) was used as the light source. A circulating water condensation system was added at the sapphire window of the reactor to eliminate the photothermal effect caused by the xenon lamp. In a typical test, the catalyst is first ordered in the raw gas environment at room temperature, and a mass flowmeter controls the flow rate of the raw gas. After 30 minutes of purging, the reactor temperature was raised to the required reaction temperature. After 60 minutes of stabilization, the light source is turned on, and the photothermal reaction begins. The output gas was analyzed in real-time using gas chromatography (GC, Agilent). Quantitative analysis of the gas-phase products was performed utilizing FID and TCD detectors. For non-permanent gas detection, add a gas washing device at the outlet of the output gas, condense and collect the non-permanent gas with 10 mL water, and conduct qualitative detection by gas chromatography and liquid chromatography.

2.4. Computational methods

The theoretical calculations were performed employing the density functional theory (DFT) as implemented in the Vienna ab initio simulation package (VASP). The interaction between ions and electrons was elucidated using the frozen-core all-electron projector-augment-wave (PAW) method. The impact of exchange-correlation was taken into account using the widely accepted Perdew-Burke-Ernzerhof (PBE) scheme within the standard generalized gradient approximation (GGA). The energy cut-off for the plane-wave basis was set at 400 eV. The Monkhorst-Pack k-points grids were utilized for Brillouin zone integration, with a resolution of 0.2 $Å^{-1}$. A vacuum slab of 15 Å was built to avoid the fictitious interactions between the supercell and its periodic images. To minimize the interaction between periodic images, we incorporated dipole corrections. Additionally, we employed the Grimme DFT-D3 dispersion correction with Becke-Jonson damping to accurately account for weak van der Waals (VDW) interactions. For structural

relaxation, we set the criteria for force and energy difference at 0.005 eV/Å and 1.0×10^{-6} eV, respectively.

3. Results and discussion

3.1. Structural characterization of catalysts

The Cu-Co-B ternary catalyst was initially synthesized using a facile chemical reduction method employing dimethylamine-borane (DMAB) as both a reducing agent and B source. Generally, the Co precursor cannot be reduced individually by DMAB at 30℃ because of the low redox potential of Co (Co^{2+}/Co: −0.227 V vs. RHE) (Fig. S3a). In contrast, the Cu precursor can be readily deposited with the assistance of DMAB at 30℃ owing to its high redox potential (Cu^{2+}/Cu: +0.340 V vs RHE) (Fig. S3b). For the mixture of Cu^{2+} and Co^{2+} solution, we proposed that Cu^{2+} species were firstly reduced as crystal seeds, subsequently triggering the co-reduction of Co^{2+}, resulting in the formation of Cu-Co-B ternary catalysts. This seeded growth in discrete steps prevents the aggregation of the catalysts and can also wrap Co species on Cu species through the boron as a bridge, forming the heterostructure.[19] After washing by centrifugation, the obtained sample was dried in air for 12 hours for partial oxidation.

The morphology and structure of the typical catalyst were initially characterized by TEM. The $CuCo_5BO_x$ catalyst primarily comprises the aggregated nanoparticles with the black dots of Cu species (Fig. 1a). The high-resolution transmission electron microscopy (HRTEM) images (Fig. 1b) indicated clear lattice fringes of 0.179 nm, corresponding to the Cu(200) plane. No crystal fringe was observed at the edge of the sample, indicating the presence of the amorphous $CoBO_x$ and confirming the outer shell of the Co species and the inner Cu species. This integrated structure enables $CuBO_x$ to work as electron donors to $CoBO_x$, making it exceptionally active for the photothermal-driven RWGS reaction. Elemental mapping images show homogeneous dispersion of Cu and Co over the samples (Fig. c-e). The concentrations of Cu, Co, and B in samples with different compositions were determined by ICP-OES in Table S1, aligning with the feed amounts. The B content increases with the rise in Co due to the higher boron solubility of cobalt compared to copper.[15,20,21]

The phase structures of as-prepared samples were carried out by XRD measurement. In Fig. 2a, the two obvious diffraction peaks at $2\theta = 43.32^\circ$ and 50.47° align with the metallic Cu, suggesting that the existence of Cu^0 in the $CuBO_x$ sample. In addition, the diffraction peak of Cu_2O (111) was also observed in $CuBO_x$, confirming the mixed valence state of $CuBO_x$ with Cu^+ and Cu^0.[22] Only a broad peak was observed for the $CoBO_x$ sample, which is the typical feature of an amorphous structure. Since the $CoBO_x$ is an amorphous structure, the $CuCo_5BO_x$ composites exhibited a similar XRD pattern with $CuBO_x$ with mixed phases of Cu_2O and Cu. Notably, the characteristic peaks observed in the Cu(111) plane of $CuBO_x$ and $CuCo_5BO_x$ discover a lower angle shifts slightly compared to commercial copper nanoparticles (Fig. 2a, inset), proving the successful incorporation of B with CuO_x. The existence of B was further verified through XPS (Fig. 2b). The bind energy of B 1 s in $CuCo_5BO_x$ was 191.9 eV, which was assigned to the peak of B-O. The binding energies of B-O for $CuCo_5BO_x$ sample surface exhibits a 0.7 eV upward shift in comparison to $CuCo_5BO_x$ after Ar^+ etching, indicating an increase the oxidation degree with the sample surface.[18] In the XPS spectra of $CuCo_5BO_x$, the Cu $2p_{3/2}$ peak is deconvoluted into two peaks at 932.3 and 934.3 eV, corresponding to Cu^0/Cu^+ and Cu^{2+}, respectively (Fig. 2c). The satellites at 941.5 eV for Cu adjacent to the main peak indicated the presence of Cu^{2+} in the samples, likely due to the spontaneous oxidation surface in the atmosphere of the air.[23,24] The Cu LMM auger electron spectra of $CuCo_5BO_x$ (Fig. 2d) exhibited a peak at 570.2 eV, suggesting the existence of Cu^+ species in $CuCo_5BO_x$.[25] The XPS spectrum of Cu in $CuCo_5BO_x$ using the Ar^+ technique confirmed the Cu^+ species exist not only on the surface but also within the samples. The Cu^+ is primarily due to electron transfer from the Cu species to the boron, consequently increasing the concentration of Cu^+. In Fig. 2e, there are no significant differences in the ratio of Co^{2+} and Co^{3+} before and after Ar^+ etching. The peaks exhibiting binding energies of 780.8 eV and 796.6 eV correspond to the Co $2p_{3/2}$ and Co $2p_{1/2}$ orbitals of Co^{3+}, while the peaks at 782.4 eV and 797.9 eV were attributed to the Co $2p_{3/2}$ and Co $2p_{1/2}$ orbitals of Co^{2+}.[26,27] The BET measurements (Fig. 2f and Table S2) indicated the addition of boron could effectively enhance the specific surface area of the catalyst.

3.2. The activity of photothermal CO_2 hydrogenation

The performances of $CuCo_yBO_x$ and reference samples were

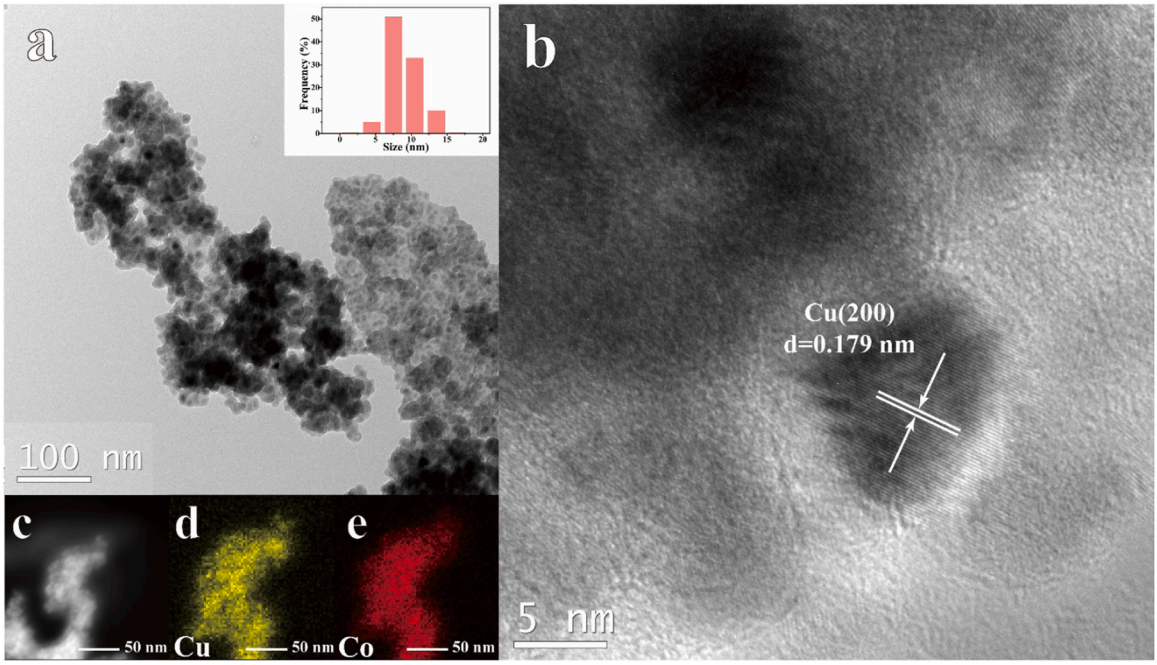

Fig. 1. (a) TEM, (b) HRTEM images, and (c-e) element mappings of $CuCo_5BO_x$.

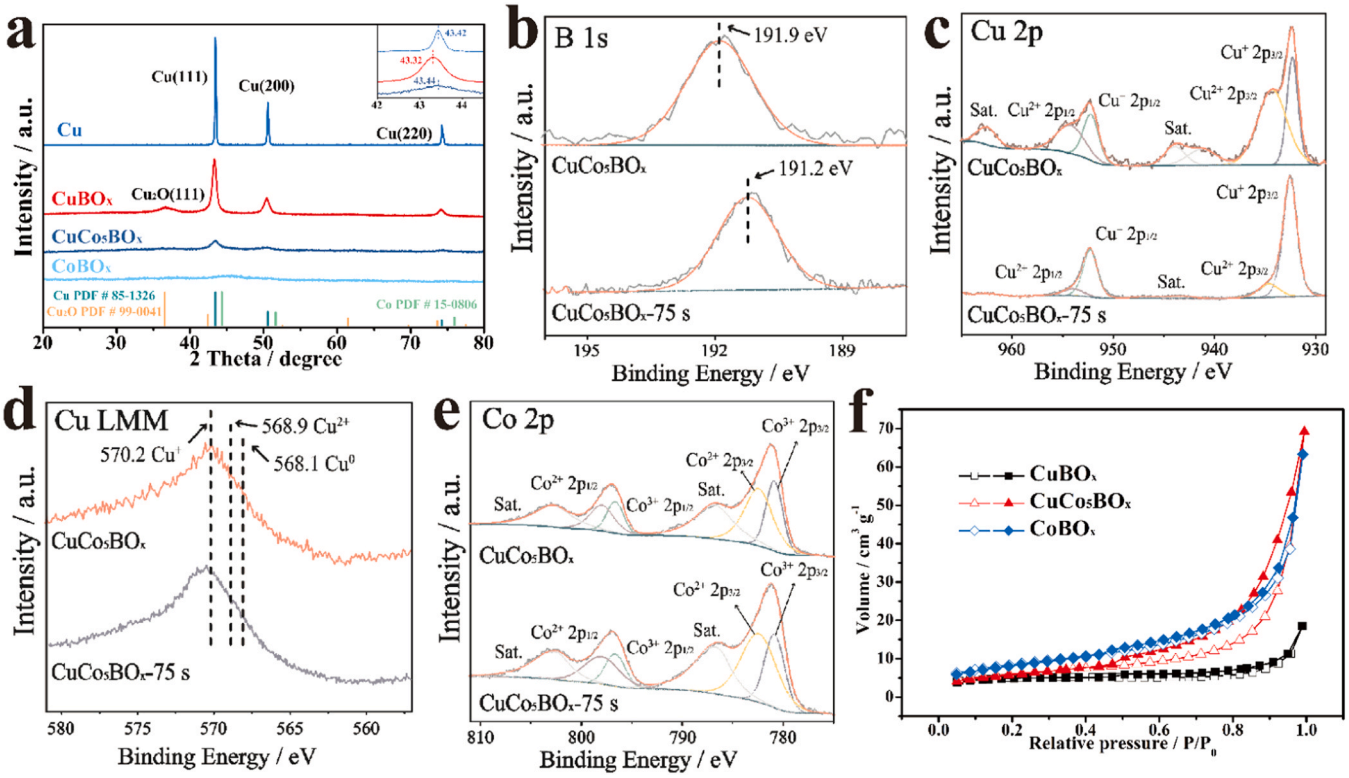

Fig. 2. (a) XRD patterns of Cu, $CuBO_x$, $CuCo_5BO_x$, and $CoBO_x$, XPS spectra of the (b) B 1 s, (c) Cu 2p, (d) Cu LMM, and (e) Co 2p levels of $CuCo_5BO_x$ and $CuCo_5BO_x$ of Ar^+ etching, (f) nitrogen asorption-desorption isotherms of $CuBO_x$, $CuCo_5BO_x$, and $CoBO_x$.

evaluated for photothermal CO_2 hydrogenation reaction in a flow-system within the temperature range of 170–300℃ (external heat source) and light. Based on the present analysis method, CO and CH_4 products were detected by GC (Fig. S4). No products were discerned in the absence of catalysts or CO_2, signifying that the catalysts activated H_2 and CO_2, and the input of CO_2 served as the sole carbon source, respectively (Fig. S5). As depicted in Fig. 3a, the catalytic performance showed a high dependence on the composition of the catalysts,

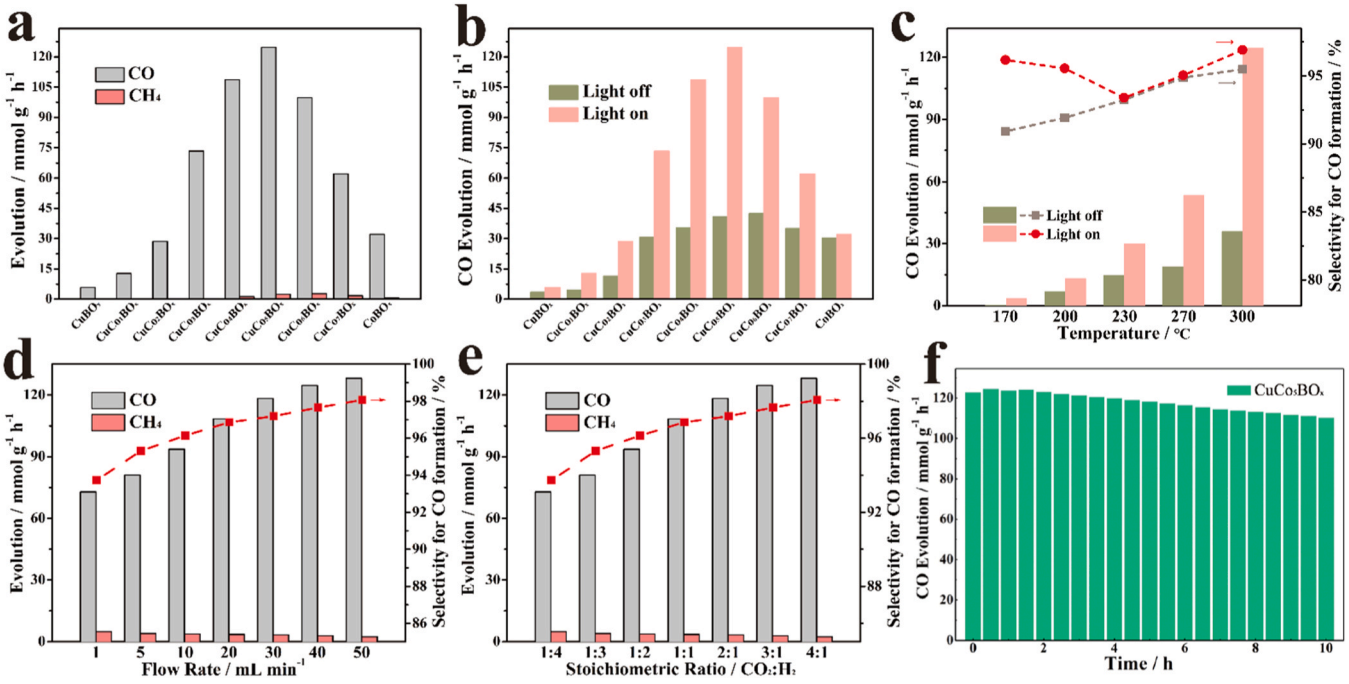

Fig. 3. Performances of different photothermal catalytic reactions in CO_2 hydrogenation by changing (a) catalysts, (b) in the presence of illumination or without illumination with different catalysts, (c) different reaction temperatures over $CuCo_5BO_x$ catalyst, (d) different flow rates of reactants in $CuCo_5BO_x$, (e) different molar ratios of CO_2:H_2 in $CuCo_5BO_x$, and (f) The stability of $CuCo_5BO_x$. (Unless otherwise stated, the reaction condition is fixed: 20 mg catalyst, 300℃ reaction temperature, 500 mW cm^{-2} light intensity, 50 mL min^{-1} flow rate, the stoichiometric ratio of CO_2:H_2 is 4:1, and 1 h reaction period.).

presenting a volcano-like trend with an increased ratio of Co species. The optimized $CuCo_5BO_x$ catalysts demonstrated the highest activity with a CO yield rate of 124.7 mmol g^{-1} h^{-1} and selectivity of 98% under photothermal catalysis. In contrast, the $CuBO_x$ catalyst displayed significantly lower activity with a CO yield rate of 5.8 mmol g^{-1} h^{-1} at the same condition, indicating the inefficiency of CO_2 hydrogenation. Pure $CoBO_x$ catalysts exhibited a low CO yield rate (32.2 mmol g^{-1} h^{-1}) compared with $CuCo_yBO_x$, showing that the $CuBO_x$ was the promoters for the reaction.

The CO yield rate of various catalysts under thermal catalytic and photothermal conditions were investigated to reveal the light effect on catalytic activity. As illustrated in Fig. 3b, a negligible increase in CO yield rate on $CoBO_x$ catalysts was observed after the introduction of light. In contrast, the CO yield rate of $CuCo_yBO_x$ catalysts increased significantly with the introduction of light, demonstrating that $CuBO_x$ could substantially enhance the overall activity of CO hydrogenation under irradiation. In Fig. 3c, it is notable that the CO yield on $CuCo_5BO_x$ catalyst increased as the temperature rose from 170℃ to 300℃, while $CuCo_5BO_x$ catalysts show no activity in the presence of light irradiation at room temperature (Fig. S5a). This suggests that photothermal CO_2 hydrogenation was dominantly a thermal-driven process.[28] After the introduction of light, the yield of CO was greatly improved, indicating that the photoinduced carriers from the $CuBO_x$ species could be transferred to the active center of $CoBO_x$, benefitting the activation of H_2 and CO_2. The UV–vis spectrum analysis of $CuCo_5BO_x$ at various temperatures was in accordance with this finding. (Fig. S6). It provided additional evidence that the rise in temperature amplifies the capacity for absorption of $CuCo_5BO_x$ of visible light. The CO selectivity of the thermo/photothermal reaction at different temperatures presents an interesting phenomenon. In thermal catalysis, CO selectivity increases monotonically with the increase in temperature due to the endothermic property of RWGS. The high temperature is more favorable to the generation of CO than CH_4. The CO selectivity of the photothermal reaction showed a V-shaped change. It is speculated that the V-shape change with the temperature increase was due to the transition from an initial kinetically controlled regime to a thermodynamically controlled regime.[19] It is concluded that photothermal catalysis appears to enhance CO selectivity and catalytic activity more effectively than pure thermal catalysis. Product yield rate of $CuCo_5BO_x$ catalysts with different light intensities were examined, revealing a monotonic increase with light intensity (Fig. S7a). The product yield rate over $CuCo_5BO_x$ catalyst at different wavelengths was also studied at 300℃ under Xe lamp irradiation using different filters. As shown in Fig. S7b, the CO yield rate decreased with the increased wavelengths, indicating that visible-light-excited carriers contributed to the high activity. In Fig. 3d, it is evident that the flow velocity of the reactant impacts both the CO yield rate and the CO selectivity. Fig. 3e further demonstrates that the CO product yield and the selectivity of $CuCo_5BO_x$ in CO_2 hydrogenation gradually increased with an elevated CO_2/H_2 ratio.

3.3. Durability

The stability test of $CuCo_5BO_x$ was performed at 300 °C under irradiation in the flow reactor. Fig. 3f shows a slight decline in the CO yield rate after 10 h, indicating superior activity and durability. HRTEM images and XRD pattern of the spent catalyst revealed that the morphology and crystal phase of the catalyst remained unchanged after a reaction time of 10 h (Fig. S8 and S9). The chemical state of the Co borides in the catalyst remained largely unchanged after the reaction (Fig. S10b and Fig. 2d), which may be the reason for the good stability of the catalyst. However, XPS pattern indicated that the proportion of Cu^+ species reduced significantly on $CuCo_5BO_x$ after a 10-hour reaction, potentially due to the high-temperature hydrogen-containing atmosphere (Fig. S10a). After the reaction for 10 h, the catalyst's activity was compared with that of the fresh catalyst by dark/light conditions (Fig. S11). The decreased activity of the used catalyst confirmed that the Cu^+ partially improves photocatalytic activity. Finally, the obtained $CuCo_5BO_x$ catalyst stored for one year still exhibited a CO yield rate as high as 88.1 mmol g^{-1} h^{-1}, indicating high stability (Fig. S12). Combining its easy storage and recovery owing to strong magnetic properties (Fig. S13), obtained $CuCo_5BO_x$ catalysts are anticipated to exhibit significant potential in heterogeneous industrial catalysis.

3.4. The role of boron-oxygen species in photothermal CO_2 hydrogenation

In order to elucidate the benefits of boron-oxygen species in $CuCo_5BO_x$ catalysts for photothermal CO_2 hydrogenation, activity tests of different samples were performed. In Fig. S14a, Cu-Co, $CuCo_5B$ and $CuCo_5O_x$ catalysts displayed the much lower CO yield rate than $CuCo_5BO_x$ catalysts, indicating that boron-oxygen incorporation notably impacted the catalytic performances remarkably. The higher activity of B-O species doped catalyst may be due to: (1) the excellent CO_2 adsorption capacity of B-O species[29]; (2) B-O species accelerated charge transfer via the intimate interfaces between the $CuBO_x$ and $CoBO_x$ species.

Firstly, the increased activity was ascribed to the excellent CO_2 adsorption of boron-oxygen species in $CuCo_5BO_x$ catalysts, as confirmed by the CO_2-TPD (Fig. S14b). The CO_2 adsorption and desorption temperature of catalysts containing B shifted significantly to high temperature (> 400℃), indicating the strong interaction of CO_2 on the surface of boron-oxygen species in $CuCo_5BO_x$ catalysts.[30,31]

Then, B-O facilitates the charge transfer between $CuBO_x$ and $CoBO_x$, which has been elucidated through a series of photochemical characterizations. As expected, the photocurrent response curves obtained under Xe lamp irradiation (Fig. S15a) confirmed the significantly low photocurrent density exhibited by $CuCo_5O_x$.The $CuCo_5BO_x$ gradually increased the photocurrent density. The UV–vis (Fig. S15b) demonstrated that the $CuCo_5BO_x$ had an ultrahigh absorbance in wide wavelength range compared to $CuCo_5O_x$. The EIS spectra (Fig.S15c) demonstrated that the introduction of B-O species doped catalyst resulted in a reduction in arc radius, indicative of an enhanced rate of electron transfer.

Photoluminescence (PL) devices were utilized to investigate the dynamics of charge carriers further.[32–34] The steady-state PL spectra at room temperature revealed that the introduction of boron effectively suppressed the recombination of electron-hole pairs (Fig. S16a). This facilitated the efficient separation of charge carriers on $CuCo_5BO_x$. The time-resolved PL decay curves for $CuCo_5BO_x$ showed an extended lifetime of charge carriers compared to $CuCo_5O_x$. The fitting analysis employed double exponential functions for both materials (Fig. S16b).[35,36] Therefore, we proposed that the B-O species as CO_2 adsorption sites in the present photothermal catalysis could facilitate the charge transfer *via* the interaction effect between the $CuBO_x$ and $CoBO_x$ species.

3.5. DFT calculations

As mentioned above, the $CuCo_5O_x$ catalyst with B-O species had excellent CO_2 hydrogenation activity due to its excellent CO_2 adsorption and accelerated charge transfer ability between the $CuBO_x$ and $CoBO_x$ species. Firstly, DFT calculation was carried out to investigate the CO_2 adsorption energy of $CuCoO_x$ and $CuCoBO_x$. As shown in Fig. S17a, the $CuCoBO_x$ catalyst with B-O species had a higher CO_2 adsorption energy, indicating excellent CO_2 adsorption capacity of B-O species. And the projected density of states (PDOS) was initially conducted to investigate the impact of B on the energy level of cobalt's *d*-orbital and CO_2 adsorption. The calculated *d*-band centers for $CuCoBO_x$ and $CuCoO_x$ were 1.05 eV and 1.16 eV (Fig. S18), respectively, indicating that the doped B species enable the *d*-band center of Co close to the Fermi energy (Ef).[37] This upshift in the *d*-band centers of $CuCoBO_x$ is advantageous for CO_2 adsorption.[38] This was consistent with the result of CO_2-TPD.

Next, to gain a comprehensive understanding of the carrier transfer model at the interface, the charge density difference was depicted in

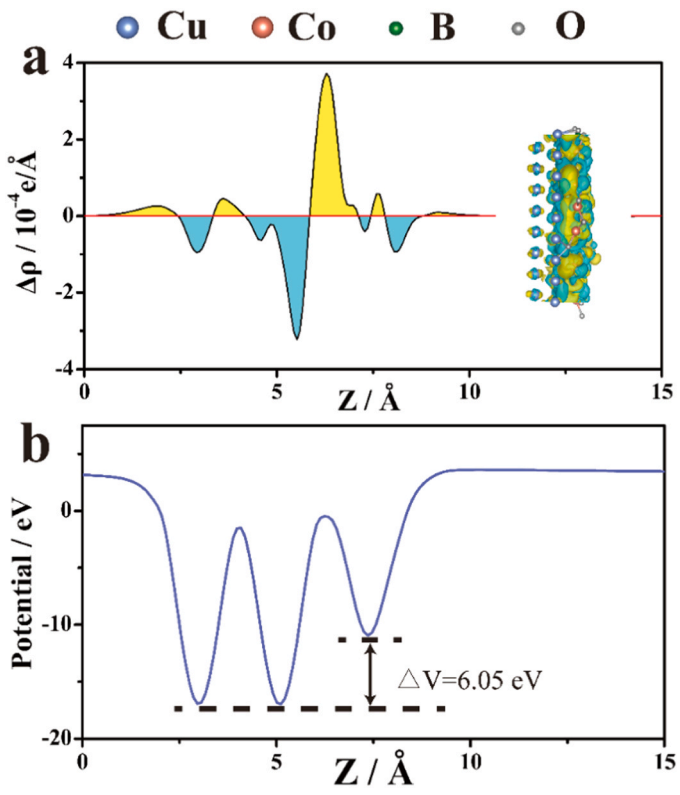

Fig. 4. (a) Plane-averaged charge density difference for the $CuCoBO_x$ along the z-axis. (b) Electrostatic potential of the $CuCoBO_x$.

Fig. 4. As seen from Fig. 4a, regions colored in yellow (representing positive values) and cyan (representing negative values) signify the accumulation and depletion of electrons, respectively. At the interface, there was an accumulation of electrons observed at the monolayer of $CoBO_x$ species (highlighted in yellow), while a depletion of electrons is observed at the monolayer of $CuBO_x$ species (highlighted in cyan). This suggests that electron transfer occurs from the layer of $CuBO_x$ species to the layer of $CoBO_x$ species.[39] Next, we conducted calculations to determine the electrostatic potential of $CuCoBO_x$ averaged over the plane in the z-direction (Fig. 4b). The results indicated that the $CuBO_x$ species monolayer has a shallower potential than the $CoBO_x$ species monolayer, driving electrons to move from the $CuBO_x$ species layer to the $CoBO_x$ species layer, which is in accord with the results from charge density difference calculations.[39] Furthermore, it was evident from Fig. 4b that there exists a significant disparity in potential energy of 6.05 eV across the interface, indicating a built-in electric field formed at the interface. In Fig.S17b, the plane-averaged electrostatic potential of the comparison $CuCoO_x$ was also calculated to show a lower built-in electric field difference than $CuCoBO_x$. And the PDOS of different elements (Fig. S19) can be shown that Cu and Co were dominantly contributed by the *d* orbital, and B was large contributed by the *p* orbital. Finally, the *p-d* orbital hybridization was the main reason for accelerating the charge transfer.[40]

Indeed, such a conclusion is consistent with our proposed mechanism, in which $CuBO_x$ species provide hot carriers through light energy. B-O species transfer hot carriers to the active center $CoBO_x$ species, which provide the active center of RWGS reaction, activating CO_2 molecules.

3.6. Study on the catalytic mechanism of photothermal CO_2 hydrogenation

The possible reaction routes of RWGS reaction were investigated using DRIFT, and its spectrum is presented in Fig. 5. When the reaction gases (CO_2 and H_2) were introduced on the $CuCo_5BO_x$, only the CO_2 absorption band appeared on the spectrum under light conditions at 25℃. It further indicates that photothermal CO_2 hydrogenation was dominantly a thermal-driven process. The monitoring of the adsorption process was conducted following a temperature rise from 25 to 200℃, during which the presence of CO_2^- (1020 and 848 cm^{-1}) and HCO_3^- (1630 and 1304 cm^{-1}) was observed in the absence of light irradiation.[41–43] The peaks' intensity has been progressively enhanced as the reaction temperature increases. It was worth mentioning that upon prolonging the irradiation time, new peaks emerge at 1220 and 1522 cm^{-1}, which can be attributed to *COOH. These newly formed peaks gradually strengthen, indicating the significant role of *COOH as an intermediate in the photocatalytic reduction of CO_2.[41–43]

The DRIFT spectra with/without light was carried out on $CuCo_5BO_x$ to investigate the impact of irradiation on the reaction path. The spectra obtained are shown in Fig. 5b. Thus, the peak at 1220 and 1522 cm^{-1} belongs to *COOH.[25,28,44,45] Compared with the dark spectrum, the peak related to *COOH increases with light introduction, which confirms that introduction of light could improve the activity through photoinduced thermal carriers.

The above discussion leads to the proposal of a photothermal RWGS reaction mechanism over the $CuCo_yBO_x$ catalyst, as shown in Fig. 6. With the assistance of thermal energy, CO_2 gas adsorbed on the boron oxide surface is activated by the active center $CoBO_x$ species. The H_2 dissociated on the surface of the $CuCo_yBO_x$ species, resulting in the overflow of the H species, which reacted with CO_3^{2-} to form bidentate

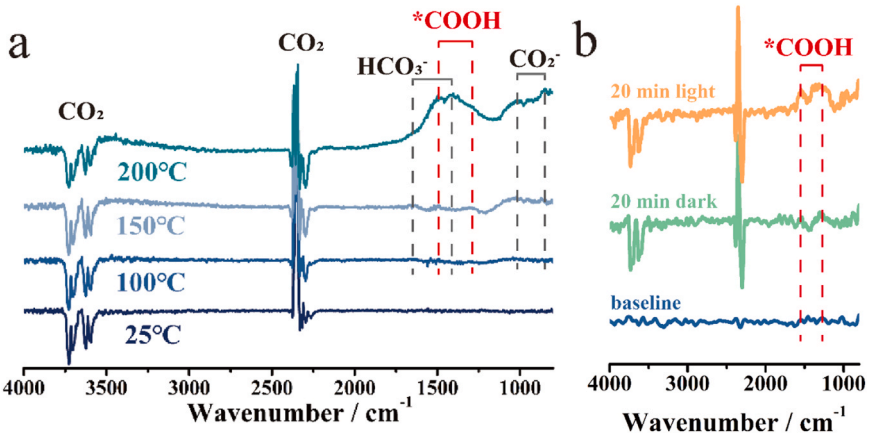

Fig. 5. In-situ DRIFT spectra on $CuCo_5BO_x$ of (a) different temperatures with irradiation in raw gas atmosphere. (b) different times with/without irradiation in raw gas atmosphere. (H_2 (5 mL min^{-1}), CO_2 (10 mL min^{-1}) and He (10 mL min^{-1})).

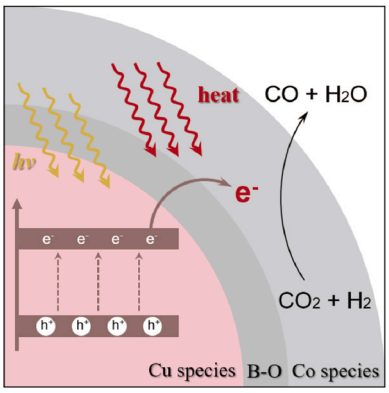

Fig. 6. Mechanism diagram of CO_2 hydrogenation with $CuCo_yBO_x$.

formate ($HCOO^-$) and finally decomposed into CO. Under light irradiation, the mixed valence of the $CuBO_x$ species could generate hot carriers. These hot carriers enhanced the dissociation of H and transferred to the active center $CoBO_x$ species through the B-O channel, thus further activating CO_2 molecules and accelerating the reduction of CO_2 and H_2.

4. Conclusion

In summary, we synthesized a series of $CuCo_yBO_x$ samples with different Cu/Co ratios using a simple chemical reduction method. Beside the high selectivity (98%), the optimized catalyst displayed 124.7 mmol g^{-1} h^{-1} CO yield rate in CO_2 hydrogenation at 300℃ with light, which was 3 times greater compared to that under thermal conditions. The $CoBO_x$ worked as the active sites for catalyzing CO_2 activation and the subsequent hydrogenation. The $CuBO_x$ acted as a photocatalyst to donate electrons to $CoBO_x$ catalyst under light irradiation, and boron-oxygen species could accelerate electron transfer. The bifunctional photothermo-catalyst demonstrated exceptional activity and selectivity in the hydrogenation of CO_2, thereby presenting a promising approach for designing cost-effective photothermal catalysts that enable efficient CO_2 hydrogenation under mild conditions.

CRediT authorship contribution statement

Shuangjun Li: Data curation. **Jiaqi Wang:** Writing – original draft, Investigation, Formal analysis, Data curation. **Kaihong Liu:** Visualization, Investigation. **Jingjing Zhao:** Resources, Investigation. **Hexing Li:** Writing – review & editing, Supervision, Funding acquisition, Conceptualization. **Bo Jiang:** Writing – review & editing, Supervision, Formal analysis, Data curation, Conceptualization.

Declaration of Competing Interest

All authors have read this manuscript and approve of its submission. The authors declare no competing interests.

Data availability

Data will be made available on request.

Acknowledgments

This work was supported by the National Key Research and Development Program of China (2020YFA0211004), the National Natural Science Foundation of China (22236005, 22106106), and the Foundation from Shanghai Local Government (22dz1205400, 21ZR1446600, 22010503400, 23520711100). This work was also sponsored by the Shanghai Engineering Research Center of Green Energy Chemical Engineering and Energy Science and Technology discipline under the Shanghai Class IV Peak Disciplinary Development Program.

Supporting Information

Supporting Information is available from the Elsevier Online Library or the author.

Appendix A. Supporting information

Supplementary data associated with this article can be found in the online version at doi:10.1016/j.apcatb.2024.124045.

References

[1] M. Bowker, S. DeBeer, N.F. Dummer, G.J. Hutchings, M. Scheffler, F. Schüth, S. H. Taylor, H. Tüysüz, Advancing critical chemical processes for a sustainable future: challenges for industry and the Max Planck–Cardiff centre on the fundamentals of heterogeneous catalysis (FUNCAT), Angew. Chem. Int. Ed. 61 (2022) e202209016, https://doi.org/10.1002/anie.202209016.
[2] C.M. Friend, B. Xu, Heterogeneous catalysis: a central science for a sustainable future, Acc. Chem. Res. 50 (2017) 517–521, https://doi.org/10.1021/acs.accounts.6b00510.
[3] D.F. Swearer, H. Zhao, L. Zhou, C. Zhang, H. Robatjazi, J.M.P. Martirez, C.M. Krauter, S. Yazdi, M.J. McClain, E. Ringe, E.A. Carter, P. Nordlander, N.J. Halas, Heterometallic antenna–reactor complexes for photocatalysis, PNAS, 113 (32) 8916-8920. https://doi.org/10.1073/pnas.1609769113.
[4] X. Meng, L. Liu, S. Ouyang, H. Xu, D. Wang, N. Zhao, J. Ye, Nanometals for solar-to-chemical energy conversion: from semiconductor-based photocatalysis to plasmon-mediated photocatalysis and photo-thermocatalysis, Adv. Mater. 28 (2016) 6781–6803, https://doi.org/10.1002/adma.201600305.
[5] X. Meng, T. Wang, L. Liu, S. Ouyang, P. Li, H. Hu, T. Kako, H. Iwai, A. Tanaka, J. Ye, Photothermal Conversion of CO_2 into CH_4 with H_2 over Group VIII nanocatalysts: an alternative approach for solar fuel production, Angew. Chem. Int. Ed. 126 (2014) 11662–11666, https://doi.org/10.1002/ange.201404953.
[6] A.P.Y. Wong, W. Sun, C. Qian, F.M. Ali, J. Jia, Z. Zheng, Y. Dong, G.A. Ozin, Tailoring CO_2 reduction with doped silicon nanocrystals, Adv. Sustain. Syst. 1 (2017) 507–511, https://doi.org/10.1002/adsu.201700118.
[7] K. Peng, J. Ye, H. Wang, H. Song, B. Deng, S. Song, Y. Wang, L. Zuo, J. Ye, Natural halloysite nanotubes supported Ru as highly active catalyst for photothermal catalytic CO_2 reduction, Appl. Catal. B-Environ. 324 (2023) 122262, https://doi.org/10.1016/j.apcatb.2022.122262.
[8] J. Ma, T. Liu, G. Chen, S. Liu, W. Gong, Y. Bai, H. Liu, Y. Wang, D. Liu, R. Long, Y. Li, Y. Xiong, Tuning the selectivity of photothermal CO_2 hydrogenation through photo-induced interaction between Ni nanoparticles and TiO_2, Appl. Catal. B-Environ. 344 (2024) 123600, https://doi.org/10.1016/j.apcatb.2023.123600.
[9] Z. Zhao, D.E. Doronkin, Y. Ye, J.D. Grunwaldt, Z. Huang, Y. Zhou, Visible light-enhanced photothermal CO_2 hydrogenation over Pt/Al_2O_3 catalyst, Chin. J. Catal. 41 (2020) 286–293, https://doi.org/10.1016/S1872-2067(19)63445-5.
[10] Q. Liu, J. Lin, H. Cheng, L. Wei, F. Wang, Simultaneous co-Photocatalytic CO_2 reduction and ethanol oxidation towards synergistic acetaldehyde Synthesis, Angew. Chem. Int. Ed. 62 (2023) e202218720, https://doi.org/10.1002/anie.202218720.
[11] H. Sugiyama, M. Miyazaki, M. Sasase, M. Kitano, H. Hosono, Room-Temperature CO_2 hydrogenation to methanol over air-stable hcp-PdMo intermetallic catalyst, J. Am. Chem. Soc. 145 (2023) 9410–9416, https://doi.org/10.1021/jacs.2c13801.
[12] H. Li, X. Zhang, D.R. MacFarlane, Carbon quantum dots/Cu_2O heterostructures for solar-light-driven conversion of CO_2 to methanol, Adv. Energy Mater. 5 (2015) 1401077, https://doi.org/10.1002/aenm.201401077.
[13] L.H. Zhang, Y. Jia, J. Zhan, G. Liu, G. Liu, F. Li, F. Yu, Dopant–Induced Electronic States Regulation Boosting Electroreduction of Dilute Nitrate to Ammonium, Angew. Chem. Int. Ed. 6, e202303483. https://doi.org/10.1002/anie.202303483.
[14] E. Cao, Z. Chen, H. Wu, P. Yu, Y. Wang, F. Xiao, S. Chen, S. Du, Y. Xie, Y. Wu, Z. Ren, Boron-induced electronic-structure reformation of CoP nanoparticles drives enhanced pH-universal hydrogen evolution, Angew. Chem. Int. Ed. 59 (2020) 4154–4160, https://doi.org/10.1002/anie.201915254.
[15] Y. Zhou, F. Che, M. Liu, C. Zou, Z. Liang, P. De Luna, H. Yuan, J. Li, Z. Wang, H. Xie, H. Li, P. Chen, E. Bladt, R. Quintero-Bermudez, T.-K. Sham, S. Bals, J. Hofkens, D. Sinton, G. Chen, E.H. Sargent, Dopant-induced electron localization drives CO_2 reduction to C_2 hydrocarbons, Nat. Chem. 10 (2018) 974–980, https://doi.org/10.1038/s41557-018-0092-x.
[16] A. Ignaczak, M. Adamiak, E. Santos, W. Schmickler, The mechanism of oxidation of formic acid in acidic solutions on boron-doped diamond electrodes: a quantum chemical study, ChemElectroChem 6 (2019) 2901–2907, https://doi.org/10.1002/celc.201900304.
[17] C. Liu, B. Sheng, Q. Zhou, D. Cao, H. Ding, S. Chen, P. Zhang, Y. Xia, X. Wu, L. Song, Motivating Ru-bri site of RuO_2 by boron doping toward high performance acidic and neutral oxygen evolution, Nano Res. 15 (2022) 7008–7015, https://doi.org/10.1007/s12274-022-4337-z.
[18] M. Yu, C. Weidenthaler, Y. Wang, E. Budiyanto, E. Onur Sahin, M. Chen, S. DeBeer, O. Rüdiger, H. Tüysüz, Surface boron modulation on cobalt oxide nanocrystals for electrochemical oxygen evolution reaction, Angew. Chem. Int. Ed. 61 (2022) e202211543, https://doi.org/10.1002/anie.202211543.

[19] L. Zhou, J.M.P. Martirez, J. Finzel, C. Zhang, D.F. Swearer, S. Tian, H. Robatjazi, M. Lou, L. Dong, L. Henderson, P. Christopher, E.A. Carter, P. Nordlander, N. J. Halas, Light-driven methane dry reforming with single atomic site antenna-reactor plasmonic photocatalysts, Nat. Energy 5 (2020) 61–70, https://doi.org/10.1038/s41560-019-0517-9.

[20] S. Amat, S. Busquier, J.M. Gutiérrez, M.A. Hernández, Letter to the Editor: On the global convergence of Chebyshev's iterative method, J. Comput. Appl. Math. 220 (2008) 17–21, https://doi.org/10.1016/j.cam.2007.07.022.

[21] J. Masa, P. Weide, D. Peeters, I. Sinev, W. Xia, Z. Sun, C. Somsen, M. Muhler, W. Schuhmann, Amorphous Cobalt Boride (Co_2B) as a highly efficient nonprecious catalyst for electrochemical water splitting: oxygen and hydrogen evolution, Adv. Energy Mater. 6 (2016) 1502313, https://doi.org/10.1002/aenm.201502313.

[22] H. Xiao, W.A. Goddard, T. Cheng, Y. Liu, Cu metal embedded in oxidized matrix catalyst to promote CO_2 activation and CO dimerization for electrochemical reduction of CO_2, PNAS 114 (2017) 6685–6688, https://doi.org/10.1002/anie.202211543.

[23] Z.H. He, Z.H. Li, Z.Y. Wang, K. Wang, Y.C. Sun, S.W. Wang, W.T. Wang, Y. Yang, Z. T. Liu, Photothermal CO_2 hydrogenation to hydrocarbons over trimetallic Co-Cu-Mn catalysts, Green Chem. 23 (2021) 5775–5785, https://doi.org/10.1039/d1gc01152a.

[24] B. Deng, H. Song, K. Peng, Q. Li, J. Ye, Metal-organic framework-derived Ga-Cu/CeO_2 catalyst for highly efficient photothermal catalytic CO_2 reduction, Appl. Catal. B-Environ. 298 (2021) 120519, https://doi.org/10.1016/j.apcatb.2021.120519.

[25] L. Wan, Q. Zhou, X. Wang, T.E. Wood, L. Wang, P.N. Duchesne, J. Guo, X. Yan, M. Xia, Y.F. Li, A.A. Jelle, U. Ulmer, J. Jia, T. Li, W. Sun, G.A. Ozin, Cu_2O nanocubes with mixed oxidation-state facets for (photo)catalytic hydrogenation of carbon dioxide, Nat. Catal. 2 (2019) 889–898, https://doi.org/10.1038/s41929-019-0338-z.

[26] W. Guo, J. Bi, Q. Zhu, J. Ma, G. Yang, H. Wu, X. Sun, B. Han, Highly Selective CO_2 Electroreduction to CO on Cu-Co Bimetallic Catalysts, ACS Sustain. Chem. Eng. 8 (2020) 12561–12567, https://doi.org/10.1021/acssuschemeng.0c03797.

[27] S. Zhang, Z. Xia, Y. Zou, M. Zhang, Y. Qu, Spatial intimacy of binary active-sites for selective sequential hydrogenation-condensation of nitriles into secondary imines, Nat. Commun. 12 (2021) 3382, https://doi.org/10.1038/s41467-021-23705-9.

[28] L. Wang, Y. Dong, T. Yan, Z. Hu, F.M. Ali, D.M. Meira, P.N. Duchesne, J.Y.Y. Loh, C. Qiu, E.E. Storey, Y. Xu, W. Sun, M. Ghoussoub, N.P. Kherani, A.S. Helmy, G. A. Ozin, Black indium oxide a photothermal CO_2 hydrogenation catalyst, Nat. Commun. 11 (2020) 2432, https://doi.org/10.1038/s41467-020-16336-z.

[29] G. Liu, X. Meng, H. Zhang, G. Zhao, H. Pang, T. Wang, P. Li, T. Kako, J. Ye, Elemental Boron for Efficient Carbon Dioxide Reduction under Light Irradiation, Angew. Chem. Int. Ed. 56 (2017) 5570–5574, https://doi.org/10.1002/anie.201701370.

[30] J. Yang, J. Wang, J. Zhao, Y. Bai, H. Du, Q. Wang, B. Jiang, H. Li, CO_2 conversion via dry reforming of methane on a core-shell Ru@SiO_2 catalyst, J. CO_2 Util. 57 (2022) 101893, https://doi.org/10.1016/j.jcou.2022.101893.

[31] J. Zhao, J. Wang, Y. Bai, H. Du, J. Yang, B. Yin, B. Jiang, H. Li, Mesoporous Ru(Co, Ni)B bimetallic amorphous alloy for CO_2 hydrogenation to formic acid, J. CO_2 Util. 74 (2023) 102528, https://doi.org/10.1016/j.jcou.2023.102528.

[32] X. Sun, L. Li, S. Jin, W. Shao, H. Wang, X. Zhang, Y. Xie, Interface boosted highly efficient selective photooxidation in Bi_3O_4Br/Bi_2O_3 heterojunctions, eScience 3 (2023) 100095, https://doi.org/10.1016/j.esci.2023.100095.

[33] B. Huang, X. Fu, K. Wang, L. Wang, H. Zhang, Z. Liu, B. Liu, J. Li, Chemically bonded $BiVO_4/Bi_{19}Cl_3S_{27}$ heterojunction with fast hole extraction dynamics for continuous CO_2 photoreduction, Adv. Powder Mater. 3 (2024) 100140, https://doi.org/10.1016/j.apmate.2023.100140.

[34] W. Shang, W. Liu, X. Cai, J. Hu, J. Guo, C. Xin, Y. Li, N. Zhang, N. Wang, C. Hao, Y. Shi, Insights into atomically dispersed reactive centers on g-C_3N_4 photocatalysts for water splitting, Adv. Powder Mater. 2 (2023) 100094, https://doi.org/10.1016/j.apmate.2022.100094.

[35] S. Li, H. Shang, Y. Tao, P. Li, H. Pan, Q. Wang, S. Zhang, H. Jia, H. Zhang, J. Cao, B. Zhang, R. Zhang, G. Li, Y. Zhang, D. Zhang, H. Li, Hydroxyl radical-mediated efficient photoelectrocatalytic NO oxidation with simultaneous nitrate storage using a flow photoanode reactor, Angew. Chem. Int. Ed. 62 (2023) e202305538, https://doi.org/10.1002/anie.202305538.

[36] Q. Zou, J. Qiu, Y. Zang, H. Tian, L. Venkataraman, Modulating single-molecule charge transport through external stimulus, eScience 3 (2023) 100115, https://doi.org/10.1016/j.esci.2023.100115.

[37] J. Li, L. Zhu, C. Tung, L. Wu, Engineering graphdiyne for solar photocatalysis, Angew. Chem. Int. Ed. 62 (2023) 1433–7851, https://doi.org/10.1002/anie.202301384.

[38] P. Li, J. Bi, J. Liu, Y. Wang, X. Kang, X. Sun, J. Zhang, Z. Liu, Q. Zhu, B. Han, p-d orbital hybridization induced by p-block metal-doped Cu promotes the formation of C_{2+} products in ampere-level CO_2 electroreduction, J. Am. Chem. Soc. 145 (2023) 4675–4682, https://doi.org/10.1021/jacs.2c12743.

[39] X. Huang, X. Shu, J. Li, Z. Cui, S. Cao, W. Chen, J. Yin, G. Yan, H. Zhao, J. Hu, Z. Yang, Y. Wang, DFT study on type-II photocatalyst for overall water splitting: g-GaN/C_2N van der Waals heterostructure, Int. J. Hydrog. Energy 48 (2023) 12364–12373, https://doi.org/10.1016/j.ijhydene.2022.12.146.

[40] L.-H. Zhang, Y. Jia, J. Zhan, G. Liu, G. Liu, F. Li, F. Yu, Dopant-induced electronic states regulation boosting electroreduction of dilute nitrate to ammonium, Angew. Chem. Int. Ed. 62 (2023) e202303483, https://doi.org/10.1002/anie.202303483.

[41] J. Liang, H. Zhang, Q. Song, Z. Liu, J. Xia, B. Yan, X. Meng, Z. Jiang, X.W. Lou, C. S. Lee, Modulating charge separation of oxygen-doped boron nitride with isolated Co atoms for enhancing CO_2-to-CO photoreduction, Adv. Mater. 36 (2023) 2303287, https://doi.org/10.1002/adma.202303287.

[42] X. Zu, Y. Zhao, X. Li, R. Chen, W. Shao, Z. Wang, J. Hu, J. Zhu, Y. Pan, Y. Sun, Y. Xie, Ultrastable and efficient visible-light-driven CO_2 reduction triggered by regenerative oxygen-vacancies in $Bi_2O_2CO_3$ nanosheets, Angew. Chem. Int. Ed. 133 (2021) 13959–13965, https://doi.org/10.1002/anie.202101894.

[43] J. Zhou, J. Li, L. Kan, L. Zhang, Q. Huang, Y. Yan, Y. Chen, J. Liu, S.L. Li, Y.Q. Lan, Linking oxidative and reductive clusters to prepare crystalline porous catalysts for photocatalytic CO_2 reduction with H_2O, Nat. Commun. 13 (2022) 578–589, https://doi.org/10.1038/s41467-022-32449-z.

[44] T. Yan, L. Wang, Y. Liang, M. Makaremi, T.E. Wood, Y. Dai, B. Huang, F.M. Ali, Y. Dong, G.A. Ozin, Polymorph selection towards photocatalytic gaseous CO_2 hydrogenation, Nat. Commun. 10 (2019) 2521, https://doi.org/10.1038/s41467-019-10524-2.

[45] J. Jia, H. Wang, Z. Lu, P.G. O'Brien, M. Ghoussoub, P. Duchesne, Z. Zheng, P. Li, Q. Qiao, L. Wang, A. Gu, F.M. Ali, Y. Dong, Q. Wang, K.K. Ghuman, T. Wood, C. Qian, Y. Shao, C. Qiu, M. Ye, Y. Zhu, Z.H. Lu, P. Zhang, A.S. Helmy, C.V. Singh, N.P. Kherani, D.D. Perovic, G.A. Ozin, Photothermal catalyst engineering: hydrogenation of gaseous CO_2 with high activity and tailored selectivity, Adv. Sci. 4 (2017) 1700252, https://doi.org/10.1002/advs.201700252.